The MIT Press Journals

This article is provided courtesy of The MIT Press.

To join an e-mail alert list and receive the latest news on our publications, please visit:

Murat Cenk Çavuşoğlu

cavusoglu@cwru.edu
Department of Electrical
Engineering and Computer Science
Case Western Reserve University
Cleveland, OH 44106

David Feygin

feygin@robotics.eecs.berkeley.edu
Department of Mechanical
Engineering
University of California
Berkeley, CA 94720

Frank Tendick

tendick@robotics.eecs.berkeley.edu
Department of Surgery
University of California
San Francisco, CA 94143

A Critical Study of the Mechanical and Electrical Properties of the PHANToM Haptic Interface and Improvements for High-Performance Control

Abstract

This paper presents a critical study of the mechanical and electrical properties of the PHANToM haptic interface and improvements to overcome its limitations for applications requiring high-performance control. Target applications share the common requirements of low-noise/granularity/latency measurements, an accurate system model, high bandwidth, the need for an open architecture, and the ability to operate for long periods without interruption while exerting significant forces. To satisfy these requirements, the kinematics, dynamics, high-frequency dynamic response, and velocity estimation of the PHANToM system are studied. Furthermore, this paper presents the details of how the unknown subsystems of the stock PHANToM can be replaced with known, high-performance systems and how additional measurement electronics can be interfaced to compensate for some of the PHANToM's shortcomings. With these modifications, it is possible to increase the maximum achievable virtual wall stiffness by 35%, active viscous damping by 120%, and teleoperation loop gain by 50% over the original system. With the modified system, it is also possible to maintain higher forces for longer periods without causing motor overheating.

1 Introduction

The PHANToM force-reflecting haptic interface, which was originally designed by Massie and Salisbury (1994) and subsequently commercialized by SensAble Technologies, Inc., is widely used in the haptics community in a multitude of applications due to its large workspace, low inertia, low friction, and high position-precision characteristics. Although this system has been used successfully as a haptic interface in typical virtual environment (VE) and telerobotics applications, the performance characteristics of the stock PHANToM do not meet the requirements of some high-performance applications.

In this paper, we present a critical study of the mechanical and electrical properties of the PHANToM haptic interface and improvements to overcome its limitations for applications requiring high-performance control. This work is motivated by our research group's experience using the PHANToM system in high-performance tasks in the areas of medical robotics and VE-based surgical training simulators. The main applications include

- implementation of complex control algorithms that require accurate measurements of position and velocity, as well as dynamic models of the manipulator,
- design of bilateral teleoperation control algorithms for high-fidelity telemanipulation of soft objects (Sherman, Çavuşoğlu, & Tendick, 2000; Çavuşoğlu, Sherman, & Tendick, 2002),
- high-fidelity haptic interaction with deformable objects in virtual environments (Çavuşoğlu & Tendick, 2000),
- haptic guidance for training (Feygin, Keehner, & Tendick, 2002), and
- psychophysics experiments to determine frequency-dependent force and impedance sensitivity of human subjects (Dhruv & Tendick, 2000)

Although our range of applications is very broad, the applications share five fundamental requirements. These are as follows.

- *Need for open architecture:* Because the electrical and software subsystems of the PHANToM haptic interface come as a black box, full functionality or control of the system is not allowed. Furthermore, the black box structure conceals the inner workings of the system, which may effect experimental results. This is not desirable for basic research. For example, one application is the experimental comparison of different teleoperation control algorithms; in this case, having a black box does not allow for a fair comparison or generalizable results. This is also true for psychophysics experiments because the unknown behavior of the system may color the experimental results.
- *Low-noise/granularity/latency measurements:* When attempting to implement high-performance control algorithms or provide accurate haptic feedback, it is important to have sensors that provide accurate and timely information on the state of the system because the controller uses this information to determine the appropriate control action. When the information is not accurate or has a large latency, the performance of the controlled system suffers.

- *Accurate system model:* When implementing control algorithms, it is desirable to have a model of the system. The more accurate this model is, the greater the performance that can be achieved.
- *High bandwidth:* High-fidelity telerobotics applications, such as telemanipulation of soft tissue in medical applications, require a relatively high-bandwidth closed-loop response. This is because the force and stiffness sensitivity of the human operator increases with frequency (Dhruv & Tendick, 2000).
- *Long operating periods without interruption while exerting significant forces:* For psychophysics experiments, it is necessary to apply significant forces for long periods. It is important not to interrupt the experiments because of motor overheating.

To satisfy these requirements, the PHANToM's kinematics, dynamics, high-frequency dynamic response, and velocity estimation are analyzed. Furthermore, we describe how we replaced the unknown subsystems of the stock PHANToM with known, high-performance systems and interfaced additional measurement electronics to compensate for some of the PHANToM's shortcomings.

At this point, we would like to emphasize that our target applications require relatively high performance, and we do not want to imply that the PHANToM is not adequate for most virtual reality applications. On the contrary, the system works without noticeable problems until one tries to push it to the limits of its performance envelope.

In this paper, we first derive the forward and inverse kinematics and the dynamic equations of motion assuming infinitely stiff joints and zero friction. We then discuss various limitations to the high-performance control of the PHANToM and modifications that were implemented to overcome these limitations. We then develop a theoretical and experimental transfer function model of the PHANToM hardware. Finally, we experimentally evaluate the modifications in a number of applications and discuss the generalizability of these results to other PHANToM models.
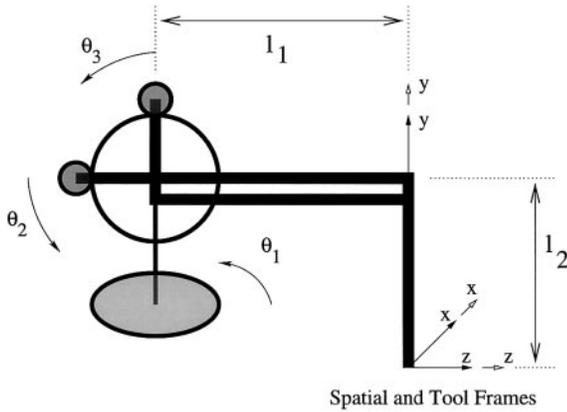
Figure 1. *Zero configuration of the manipulator.*

In this document, we will follow the notation of Murray, Li, and Sastry (1994) in representing rigid-body transformations and kinematics and dynamics calculations. Results of the calculations are also related to the notation of Craig (1989). The units are in meter-kilogram-second (MKS), unless otherwise noted. Throughout the paper, parameters and measurements are based on the PHANToM model 1.5.

2   Kinematics

In this section, the kinematic analysis of the PHANToM manipulator is performed. Although some of the results given here are already implemented in SensAble's GHOST and Basic I/O libraries, we believe it is useful to have explicit expressions for the sake of having an open architecture and to use in tasks and functions not supported in these libraries.

In the following subsections, solutions of the forward and inverse kinematics are presented, followed by the calculation of the manipulator Jacobian and a basic analysis of the workspace.

2.1 Forward Kinematics

Using the zero configuration and the naming convention shown in figure 1, the kinematic configuration
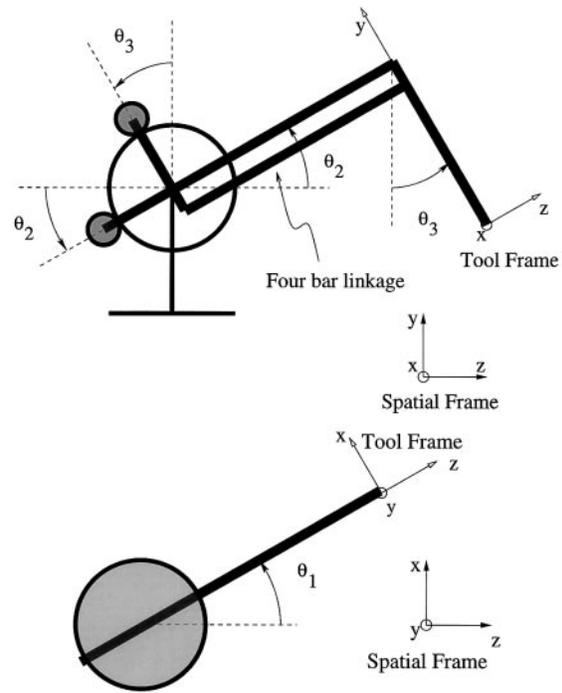
Figure 2. *Side and top views.*

of the manipulator is characterized by the following vectors and points:

$$w_1 = [\ 0 \quad 1 \quad 0 \ ]^T$$

$$w_2 = w_3 = [\ -1 \quad 0 \quad 0 \ ]^T$$

$$q_1 = [\ 0 \quad 0 \quad -l_1 \ ]^T$$

$$q_2 = q_3 = [\ 0 \quad l_2 \quad -l_1 \ ]^T$$

$$\xi_i = \left[\begin{array}{c} -w_i \times q_i \\ w_i \end{array} \right], \quad i = 1, 2, 3 \, .$$

Values for l_1 and l_2 for the PHANToM model 1.5 are given in the appendix.

It can easily be seen from the side and top view illustrations in figure 2 that the forward kinematic map is given by

$$g_{st}(\theta) = \begin{bmatrix} R(\theta) & p(\theta) \\ 0\ 0\ 0 & \end{bmatrix}$$

where

$$R(\theta) = e^{\hat{w}_1\theta_1}e^{\hat{w}_3\theta_3}I_{3\times3} \qquad (1)$$

and

$$p(\theta) = e^{\hat{\xi}_1\theta_1}e^{\hat{\xi}_2\theta_2}\begin{bmatrix} I_{3\times3} & \begin{matrix}0\\l_2\\0\end{matrix} \\ 0\ 0\ 0 & 1 \end{bmatrix}\begin{bmatrix}0\\0\\0\\1\end{bmatrix} + \begin{bmatrix} R(\theta)\begin{matrix}0\\-l_2\\0\end{matrix} \\ 0 \end{bmatrix}.$$

In closed form,

$$g_{st}(\theta) = \begin{bmatrix} \cos(\theta_1) & -\sin(\theta_1)\sin(\theta_3) & \cos(\theta_3)\sin(\theta_1) & \sin(\theta_1)(l_1\cos(\theta_2) + l_2\sin(\theta_3)) \\ 0 & \cos(\theta_3) & \sin(\theta_3) & l_2 - l_2\cos(\theta_3) + l_1\sin(\theta_2) \\ -\sin(\theta_1) & -\cos(\theta_1)\sin(\theta_3) & \cos(\theta_1)\cos(\theta_3) & -l_1 + \cos(\theta_1)(l_1\cos(\theta_2) + l_2\sin(\theta_3)) \\ 0 & 0 & 0 & 1 \end{bmatrix}$$

In the notation of Craig (1989), $^S_TT = g_{st}(\theta)$ above.

2.2 Inverse Kinematics

As this is a three-DOF manipulator, the inverse kinematics problem is to find the set of $(\theta_1, \theta_2, \theta_3)$ triples that moves the manipulator to a desired end effector position $p_o = \begin{bmatrix} p_{ox} & p_{oy} & p_{oz} \end{bmatrix}^T$. ($\theta_1$ is determined by inspection from the top view in figure 2, and θ_2 and θ_3 are determined again by inspection and using law of cosines twice on the side view.) The resulting angles are given by

$$\theta_1 = \text{atan2}(p_{ox}, p_{oz}+l_1)$$

$$d = \sqrt{p_{ox}^2 + (p_{oz}+l_1)^2}$$

$$r = \sqrt{p_{ox}^2 + (p_{oy}-l_2)^2 + (p_{oz}+l_1)^2}$$

$$\theta_2 = \cos^{-1}\left(\frac{l_1^2 + r^2 - l_2^2}{2l_1 r}\right) + \text{atan2}(p_{oy}-l_2, d)$$

$$\theta_3 = \theta_2 + \cos^{-1}\left(\frac{l_1^2 + l_2^2 - r^2}{2l_1 l_2}\right) - \frac{\pi}{2},$$

where d and r are intermediate variables.

2.3 Manipulator Jacobian

The body Jacobian of the manipulator is given by

$$J^b(\theta) = \begin{bmatrix} \cdots & \left(g_{st}^{-1}\frac{\delta g_{st}}{\delta\theta_i}\right)^v & \cdots \end{bmatrix}$$

$$= \begin{bmatrix} l_1\cos(\theta_2) + l_2\sin(\theta_3) & 0 & 0 \\ 0 & l_1\cos(\theta_2 - \theta_3) & 0 \\ 0 & -l_1\sin(\theta_2 - \theta_3) & l_2 \\ 0 & 0 & -1 \\ \cos(\theta_3) & 0 & 0 \\ \sin(\theta_3) & 0 & 0 \end{bmatrix}$$

Using the body Jacobian of the manipulator, the hybrid velocity of the tool frame (the translational and angular velocity of the tool frame, around the origin of the tool frame, expressed in spatial coordinates) is calculated as

$$V^b = \begin{bmatrix} R & 0 \\ 0 & R \end{bmatrix}J^b\dot{\theta},$$

where R is given in equation seven. In the notation of Craig (1989), $^S V = V^b$. The motor torques required to counteract the hybrid wrench F^b applied to the manipulator are given by

$$\tau = J^{bT}\begin{bmatrix} R^T & 0 \\ 0 & R^T \end{bmatrix}F^b.$$
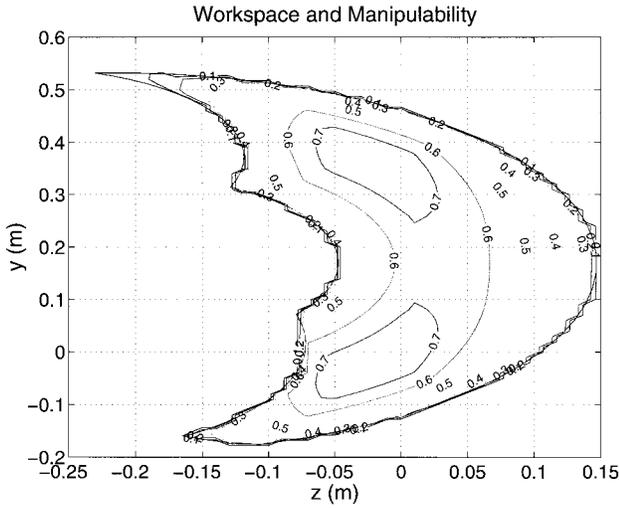
Figure 3. *Workspace and manipulability. This plot shows the cross section of the workspace and isomanipulability curves of the PHANToM at the x = 0 plane, which corresponds to $\theta_1 = 0$. Note that the kinematics are circularly symmetric for θ_1.*

The hybrid wrench is the force/torque combination applied to the origin of the tool frame expressed in spatial coordinates. In the notation of Craig (1989), $^SF = F^b$.

Figure 3 shows the workspace and the manipulability of the PHANToM. The manipulability measure used here is $\mu = \sigma_{min}(J_u^b)/\sigma_{max}(J_u^b)$, where σ_{min} and σ_{max} are the minimum and maximum singular values, and J_u^b is the upper half of the manipulator Jacobian (which corresponds to the translational part). This plot reveals that the PHANToM haptic interface has a singularity-free workspace with quite uniform manipulability over a significant portion of the workspace, which is a favorable kinematic property.

3   Dynamics

It is necessary to know the dynamic equations of motion for the manipulator to implement high-performance controllers such as gravity compensation or the computed torque control algorithm. The dynamic equations for the PHANToM manipulator are in the form

$$
\begin{bmatrix} M_{11} & 0 & 0 \\ 0 & M_{22} & M_{23} \\ 0 & M_{32} & M_{33} \end{bmatrix} \begin{bmatrix} \ddot{\theta}_1 \\ \ddot{\theta}_2 \\ \ddot{\theta}_3 \end{bmatrix}
$$

$$
+ \begin{bmatrix} C_{11} & C_{12} & C_{13} \\ C_{21} & 0 & C_{23} \\ C_{31} & C_{32} & 0 \end{bmatrix} \begin{bmatrix} \dot{\theta}_1 \\ \dot{\theta}_2 \\ \dot{\theta}_3 \end{bmatrix} + \begin{bmatrix} 0 \\ N_2 \\ N_3 \end{bmatrix} = \begin{bmatrix} \tau_1 \\ \tau_2 \\ \tau_3 \end{bmatrix}
$$

where

$$
M_{11} = \left(\frac{1}{8} \left(4I_{ayy} + 4I_{azz} + 8I_{baseyy} + 4I_{beyy} + 4I_{bezz} + 4I_{cyy} \right. \right.
$$

$$
\left. + 4I_{czz} + 4I_{dfyy} + 4I_{dfzz} + 4l_1^2 m_a + l_2^2 m_a + l_1^2 m_c + 4l_3^2 m_c \right)
$$

$$
+ \frac{1}{8} \left(4I_{beyy} - 4I_{bezz} + 4I_{cyy} - 4I_{czz} \right.
$$

$$
\left. + l_1^2 (4m_a + m_c) \right) \cos(2\theta_2)
$$

$$
+ \frac{1}{8} \left(4I_{ayy} - 4I_{azz} + 4I_{dfyy} - 4I_{dfzz} \right.
$$

$$
\left. - l_2^2 m_a - 4l_3^2 m_c \right) \cos(2\theta_3) + l_1 (l_2 m_a + l_3 m_c) \cos(\theta_2) \sin(\theta_3) \right)
$$

$$
M_{22} = \frac{1}{4} (4(I_{bexx} + I_{cxx} + l_1^2 m_a) + l_1^2 m_c)
$$

$$
M_{23} = -\frac{1}{2} l_1 (l_2 m_a + l_3 m_c) \sin(\theta_2 - \theta_3)
$$

$$
M_{32} = -\frac{1}{2} l_1 (l_2 m_a + l_3 m_c) \sin(\theta_2 - \theta_3)
$$

$$
M_{33} = \frac{1}{4} (4I_{axx} + 4I_{dfxx} + l_2^2 m_a + 4l_3^2 m_c)
$$

$$
C_{11} = \frac{1}{8} \left(-2\sin(\theta_2) \left((4I_{be_{yy}} - 4I_{be_{zz}} + 4I_{cyy} - 4I_{czz} \right. \right.
$$

$$
\left. + 4l_1^2 m_a + l_1^2 m_c)\cos(\theta_2) + 2l_1(l_2 m_a + l_3 m_c)\sin(\theta_3) \right) \dot{\theta}_2
$$

$$
+ 2\cos(\theta_3) \left(2l_1(l_2 m_a + l_3 m_c)\cos(\theta_2) \right.
$$

$$
+ (-4I_{ayy} + 4I_{azz} - 4I_{dfyy} + 4I_{dfzz} + l_2^2 m_a
$$

$$
\left. \left. + 4l_3^2 m_c)\sin(\theta_3) \right) \dot{\theta}_3 \right)
$$

$$C_{12} = -\frac{1}{8}\bigg((4I_{beyy} - 4I_{bezz} + 4I_{cyy} - 4I_{czz} + l_1^2(4m_a$$

$$+ m_c))\sin(2\theta_2) + 4l_1(l_2 m_a + l_3 m_c)\sin(\theta_2)\sin(\theta_3)\bigg)\dot{\theta}_1$$

$$C_{13} = -\frac{1}{8}(-4l_1(l_2 m_a + l_3 m_c)\cos(\theta_2)\cos(\theta_3) - (-4I_{ayy}$$

$$+ 4I_{azz} - 4I_{df_{yy}} + 4I_{df_{zz}} + l_2^2 m_a + 4l_3^2 m_c)\sin(2\theta_3))\dot{\theta}_1$$

$$C_{21} = -C_{12}$$

$$C_{23} = \frac{1}{2}l_1(l_2 m_a + l_3 m_c)\cos(\theta_2 - \theta_3)\dot{\theta}_3$$

$$C_{31} = -C_{13}$$

$$C_{32} = \frac{1}{2}l_1(l_2 m_a + l_3 m_c)\cos(\theta_2 - \theta_3)\dot{\theta}_2$$

$$N_2 = \frac{1}{2}g(2l_1 m_a + 2l_5 m_{bc} + l_1 m_c)\cos(\theta_2)$$

$$N_3 = \frac{1}{2}g(l_2 m_a + 2l_3 m_c - 2l_6 m_{df})\sin(\theta_3) \,.$$

These dynamic equations assume that the gravity vector is in the $-y$ direction. The estimated numerical values for the inertial parameters for the PHANToM model 1.5 manipulator are given in appendix A. Details of the derivation of the dynamic equations and inertial parameters can be found in Çavuşoğlu and Feygin (2001).

4 Control Issues

When pushing the PHANToM to the edge of its performance envelope, one encounters a number of limitations that impede high-performance control. In this section, some of the factors limiting the performance of the stock PHANToM system are described, and improvements that mitigate these limitations are presented. Furthermore, an accurate frequency response and system model is presented for the purpose of high-performance control.

4.1 Limitations of the PHANToM

Initial attempts at high-bandwidth position control during bilateral teleoperation with two PHANToM manipulators, using a simple PD controller, resulted in instability even at moderate gains. Furthermore, a resonance was observed at 125 Hz. The inadequate performance of the stock PHANToM during these initial attempts prompted further investigation of the PHANToM system.

4.1.1 Motor drive electronics.
The motor drive electronics come as a black box for which the system behavior is not known. This conflicts with our need for an open architecture.

It is not desirable to drive DC brush motors with voltage-regulating amplifiers on haptic devices for which one wants to servo forces. First, for DC motors, torque is proportional to current, not voltage. Second, brush DC motors (as the name implies) contain brushes, and, when these brushes switch, the resistance of the windings changes. If the amplifier regulates voltage, the change in resistance causes a change in the current, and thus a change in the motor torque. This is called *cogging,* and it contaminates the haptic feedback. With the original PHANToM amplifier box, one can feel a spatially periodic variation in force during a constant-force command. This may be attributable to motor cogging.

The amplifier box supplied with the PHANToM system uses a motor drive based on pulse width modulation (PWM). Although PWM is adequate in many applications, the high-frequency switching associated with the PWM signal makes it inadequate for high-performance applications. The PWM signal has significant power in the high-frequency range due to the switching and is therefore more likely to excite high-frequency dynamics that could lead to instability as compared to a linear signal.

The PWM power drive also increases motor overheating as compared to a linear drive. When conducting psychophysics experiments with the stock PHANToM setup, we noticed that the application of reasonable finger forces for prolonged periods with little motion caused a fault in the software due to the overheating of the motors. This problem is significantly mitigated by using linear current amplifiers. The heat dissipation in a motor is given by $I^2 R,$ where I is the motor current and R is the resistance of the motor windings. The ratio of

heat dissipation with the PWM amplifiers over the linear current amplifiers is

$$\frac{I_{\max}^2 \times \text{Duty Cycle} \times R}{(I_{\max} \times \text{Duty Cycle})^2 \times R} = \frac{1}{\text{Duty Cycle}} .$$

For example, at one fourth of full force, or 25% duty cycle, the original PWM amplifier results in four times the heat dissipation of a linear amplifier.

4.1.2 Velocity estimation. The PHANToM has a position precision of 0.03 mm at the center of the workspace (SensAble Technologies, 1997), but the granularity of velocity measurements at the haptic sampling rate of 1 kHz is $\Delta v = (\Delta x / \Delta t) = (0.03$ mm$/0.001$ sec$) = 30$ mm/sec. Although the position precision is good, this level of velocity granularity is very large, especially for a haptic interface, which will typically move at low velocities. The PHANToM Basic I/O libraries use a velocity estimate averaged over 100 samples, which results in an approximate lag of 50 ms (SensAble Technologies, Inc. 1997). This much lag can induce instability at moderate velocity gains in the control loop (50 ms of lag adds 180 deg. of phase at 10 Hz).

The mechanical system of the PHANToM has minimal damping. Therefore, it is important to have active damping with velocity feedback to stabilize the system. However, the large velocity granularity and the lag introduced from the averaging does not allow effective velocity feedback. Furthermore, many virtual environment and haptic training applications require large amounts of damping.

4.2 System improvements

The following improvements have been made to the PHANToM system to overcome the limitations described in the previous section and achieve improved performance.

4.2.1 Motor drive electronics. To overcome the limitations associated with the original PHANToM motor drive electronics (as well as to replace the black

box component with a known component), the original amplifier box is replaced with a high-performance, linear current amplifier (from Glentek, El Segundo, CA, part number GA4555). This amplifier provided more than adequate continuous power/linearity and bandwidth for high-performance control of the PHANToM. It is important to note that, when the PHANToM amplifier box is not used, the update rate and temperature control safety logic are bypassed as well. It is therefore important to implement these in the drivers for the new amplifiers.

4.2.2 Velocity estimation. A period measurement velocity estimation system, following the method proposed by Lemkin, Yang, Huang, Jones, and Auslander (1995), was developed and interfaced with the PHANToM electronics to mitigate the problem of large velocity granularity. This velocity estimation system measures the period between encoder counts. A Lattice 3320 FPGA was programmed to decode the quadrature signal to determine direction, count the number of clock ticks between pulses, and communicate to the computer through 16 bits of digital I/O. Running a 10 MHz clock with a 16-bit counter allowed more than adequate dynamic range for measurements of both small and large end effector velocities, with very little granularity. However, at low velocities, the update rate is reduced below the nominal 1 kHz because no new information is introduced to the system when there are no encoder ticks. Additional software logic was implemented to account for the low update rate and to estimate velocity more accurately. As a result of this additional software logic and the very precise period measurement, the effect of the low update rate at low velocities is imperceptible.

This system provides much more accurate velocity measurements, reducing the need for averaging the velocity readings and therefore reducing the lag in the velocity estimation. The current implementation averages sixteen velocity samples, as compared to the PHANToM's 100, reducing the lag by a factor of 6 while providing smoother and more-accurate velocity information. The number of averaged velocity measurements is very important for high-bandwidth control of

the PHANToM. The number of averaged samples must be large enough to produce smooth and accurate velocity information while remaining small enough so as not to introduce significant lag in the velocity information. The order of this averaging filter should also be a factor of 4 so that the variations in the quadrature encoder spacing do not affect the measurement. Initial attempts at using an eighth- and twelth-order averaging filter produced velocity estimation that was not adequately smooth, so a sixteenth-order filter was implemented.

4.3 Frequency Response

The frequency response of the manipulator is determined using the linear current amplifiers and a real-time operating system (a PC running the QNX operating system) running at a 10 kHz sampling rate. This rate is used instead of the standard sampling rate (1 kHz) of the PHANToM system to accurately observe high-frequency behavior. Of particular interest is the observed 125 Hz resonance previously mentioned. Because high-performance linear current amplifiers, a real-time OS, and a high sampling rate are used, the frequency response is a good representation of the actual mechanics of the PHANToM and not significantly influenced by the electronics or software.

Figure 4 shows the frequency responses of the manipulator at the origin of the workspace along the three spatial directions. In the frequency response measurements, the input was the force along the axis and the output was the measured position. During the experiments, the motion of the manipulator was constrained to the measured axis by simple proportional controllers in the orthogonal directions. The manipulator was oriented such that the measured axis was parallel to the ground plane, therefore removing the gravitational effects. The frequency response was measured at discrete frequencies. In all three axes, the frequency response at low frequencies is in the form $1/s^2$, which is the form for pure inertial behavior. The x axis has a resonance at 90 Hz. The 125 Hz resonance that was observed during control of the system with the original PHANToM amplifiers is clearly visible in the y axis frequency response. The y axis has other smaller resonances at 60 Hz

and 250 Hz, and an even smaller one at 30 Hz. The z axis resonance is at approximately 65 Hz. The reported resonance frequencies are at the origin of the workspace, and they change slightly at different locations. However, the general shapes of the frequency responses stay the same around the center of the workspace. The frequency response curves are consistently reproducible.

4.3.1 Theoretical Transfer Function Model.
We develop a simplified transfer function model for the PHANToM by making the following key assumptions: we assume that the system is linear, that the bandwidth of the electronics is very high and can be neglected, and that the mechanism consists of two lumped masses connected by a spring and a damper. The first mass is taken to be the motor, to which the force is applied. The spring and damper include the effects of flexure of the mechanism, finite stiffness of the connecting rods, finite stiffness of the wire rope tendons, frictional losses, and so on. The second mass is taken to be a lumped representation of all the mass after the motor. This model, shown in figure 5(a), gives a fourth-order transfer function with two zeros. This model is appropriate for the x axis because the θ_0 motor is attached to ground. For the y and z axis, the motors (θ_2 and θ_3) are not directly attached to ground, but are connected to ground through the wire rope tendon. This model, shown in figure 5(b), gives a fourth-order transfer function with four zeros.

The transfer function model, from force to measured position, for the x direction is then given by

$$\frac{\text{Measured Position}}{\text{Force}} = \frac{1}{s^2} \frac{m_2 s^2 + bs + k}{m_1 m_2 s^2 + (m_1 + m_2)(bs + k)}$$

The transfer function model, from force to measured position, for the y and z directions is then given by

$$\frac{\text{Measured Position}}{\text{Force}}$$

$$= \frac{1}{s^2} \frac{\begin{matrix} s^2 \left(m_1 m_2 s^2 + (m_1 + m_2)\,(bs + k) \right) \\ + k_{\text{tendon}}(m_2 s^2 + bs + k) \end{matrix}}{k_{\text{tendon}}(m_1 m_2 s^2 + (m_1 + m_2)\,(bs + k))}$$
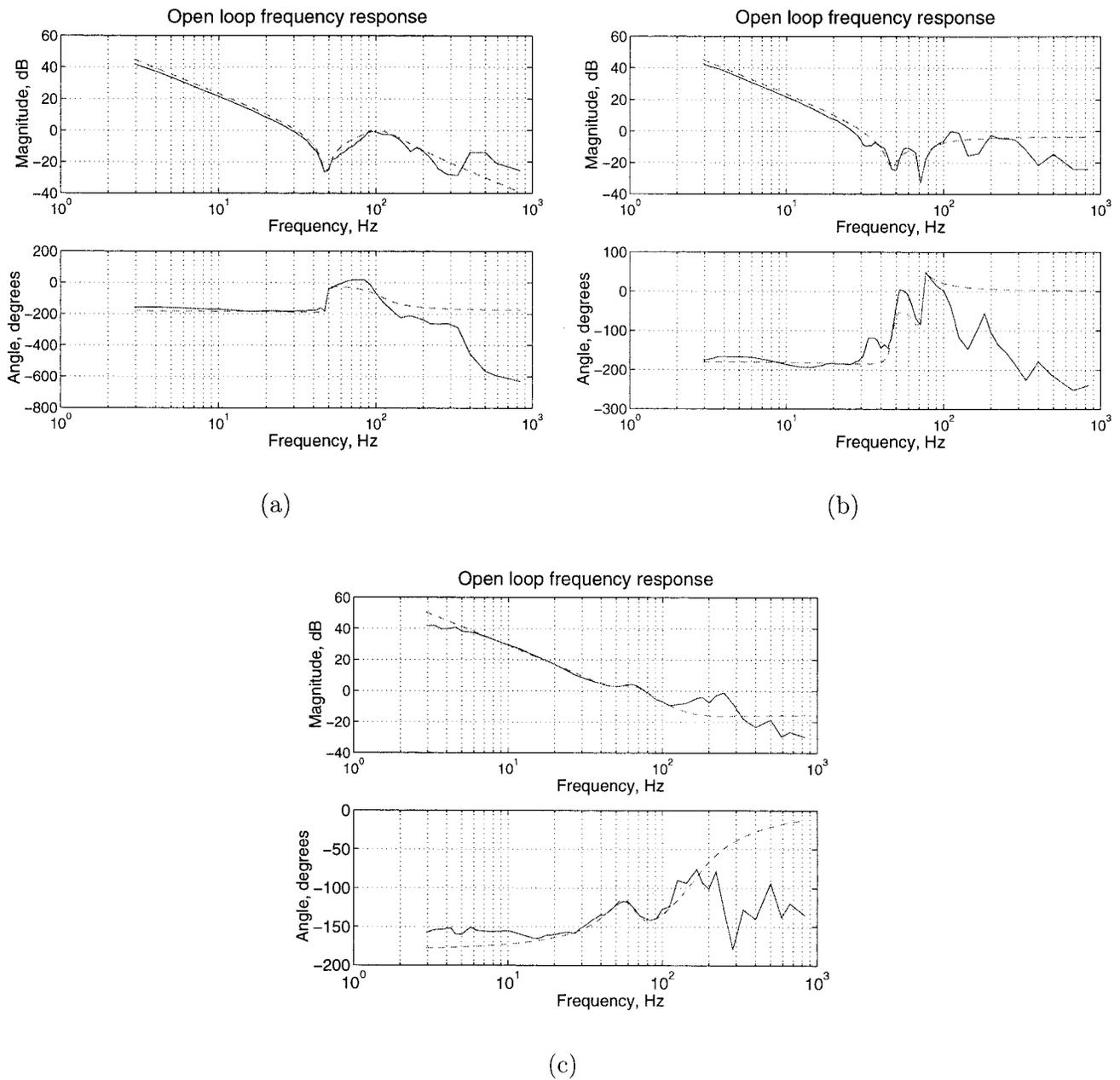
Figure 4. *Frequency response of the PHANToM at the origin with the linear model fits. (a) x axis, (b) y axis, (c) z axis. Solid curves are the experimental data, and dashed curves are the linear model fits.*

4.3.2 Experimental Transfer Function Model.

An experimental transfer function model for the PHANToM at the center of the workspace, along the three principal axes, is determined. By assuming a form for the transfer function identical to the

theoretical model[1] and fitting this transfer function to the frequency response data, we determine the experimental transfer function model to be

---

1. To simplify the computation, we used the nonparametric form of the transfer function.
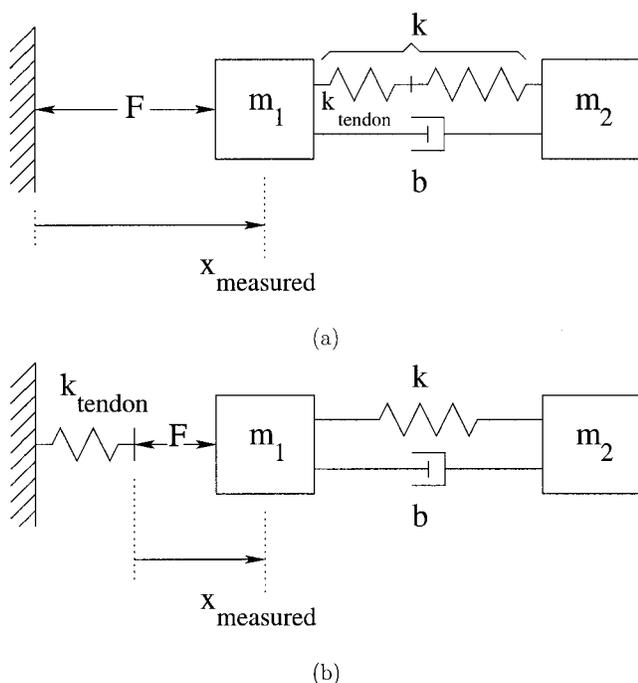
Figure 5. *Linear models of the PHANToM at the center of the workspace. (a) Along the x axis, (b) along the y and z axes.*

along the *x* axis:

$$\frac{1}{s^2} \frac{s^2 + 5.716s + 9.201 \times 10^4}{3.329 \times 10^{-6}s^2 + 0.001226s + 1.536}$$

along the *y* axis:

$$\frac{1}{s^2} \frac{s^4 + 30.25s^3 + 2.923 \times 10^5 s^2 + 5.741 \times 10^6 s + 1.784 \times 10^{10}}{1.526s^2 + 233s + 2.848 \times 10^5}$$

along the *z* axis:

$$\frac{1}{s^2} \frac{s^4 + 1248s^3 + 1.275 \times 10^6 s^2 + 3.243 \times 10^8 s + 1.097 \times 10^{11}}{5.953s^2 + 875.3s + 9.635 \times 10^5}$$

As can be seen from figure 4, these linear models closely approximate the low-frequency behavior (up to about 200 Hz) of the system. Obviously, the model has higher-order dynamics that are not considered.

5 Experimental Evaluation of the Improvements

Implementing the high-performance, linear current amplifiers eliminated the effects of motor cogging and allowed us to increase system bandwidth without exciting the resonances of the system.

For quantitative evaluation of the improvements to the PHANToM system just described, we have considered two different setups. Both of the setups were run on an SGI Octane workstation running a real-time OS extender (supplied with the PHANToM Basic I/O libraries) with a 1 kHz sampling rate. In all experiments, the maximum achievable gains were taken to be the gains that result in marginal stability of the system. Marginal stability was taken as the condition in which there were small sustained oscillations that did not grow in magnitude.

The first experimental configuration is a teleoperation setup, shown in figure 6(a) (Sherman et al., 2000). The master and slave manipulators were two identical PHANToM vl.5 manipulators. The slave manipulator had a rigid plastic hemisphere of 2 cm diameter as the end effector, and the master manipulator had a plastic stylus handle as its end effector. A pen grip was used to hold the master handle. A position-error-based force feedback controller, as shown in figure 6(b), was used as the bilateral control law. In position-error-based force feedback, the force fed back to both the master and slave manipulators is proportional to the error between the two. This is a simple and very commonly used teleoperation architecture. In this system, the loop gain was increased until the system was at least marginally stable throughout the entire workspace (in free space). With the high-performance, linear current amplifiers, it was possible to increase the loop gain of the system by 50%, compared to the original PHANToM amplifiers.

The second experimental configuration used to evaluate the improvements was a VE setup with a single PHANToM manipulator with the SensAble-supplied finger gimbal attachment. With this setup, we performed two tests. In the first test, a planar virtual wall was implemented, and the maximum stable virtual wall stiffness, without active damping, was measured. The
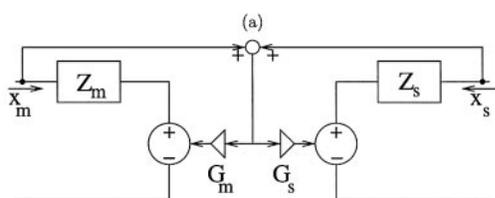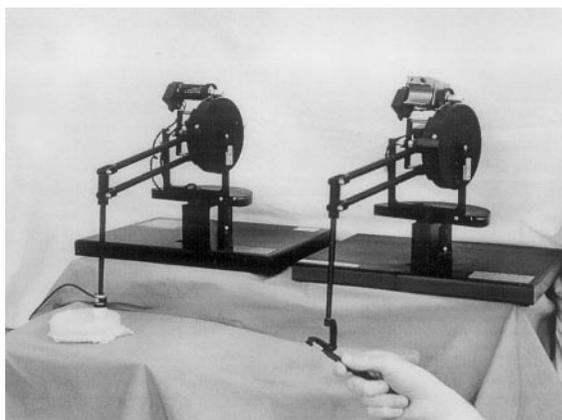
Figure 6. *(a) Teleoperation setup. (b) Block diagram of the position-error-based force feedback controller used in the teleoperation system. In the block diagram, Z_m and Z_s are the manipulator impedances, G_m and G_s are the controller gains ($G_m = G_s$ for this experiment), and x_m and x_s are the measured positions. Subscripts m and s denote master and slave, respectively.*

virtual wall was modeled as a simple Hooke's Law spring, in which the reaction force is normal to the wall and proportional to the penetration distance. The wall's normal vector pointed in the $+y$ direction, and the wall was located at $y = 0$ in PHANToM coordinates. For the original and new amplifiers, wall stiffness was gradually increased until the system was marginally stable upon wall penetration near the origin. Using the new amplifier, the maximum possible wall stiffness increased to 2.7 N/mm, as opposed to 2.0 N/mm with the original amplifiers. In the second test, we compared the effects of the improved velocity estimation. In this experimental condition, we simulated motion through a viscous liquid. A damping force proportional to the measured velocity was applied in the direction opposite the motion. The damping coefficient was gradually increased until the system was marginally stable during motion over the entire workspace. The results were dramatically

different between the original and the new setups. With the new amplifiers and the period-measurement-based velocity estimation system, the maximum stable pure viscous damping increased from 0.0050 N/(mm/s) to 0.011 N/(mm/s)—a more than twofold improvement. Furthermore, the damping felt smoother.

The problem of motor overheating, described in subsection 4.1.1, is also significantly mitigated with the use of the linear current amplifiers. With the PHANToM constrained, a constant 2 N force was applied in the $-y$ (downward) direction for 10 min. and the temperature change at the motor casing was measured. With the linear current amplifier, the motor casing temperature increased by 14.5 deg. (C) as compared to a 34.5 deg. increase with the original PHANToM PWM amplifier (at 25.6 deg. ambient temperature).

5.1 Implementing Dynamic Equations of Motion

Using the derived dynamics of the PHANToM along with the approximations of the inertial parameters of each of the links, we were able to implement a gravity compensation control scheme. The gravity compensation works very well, eliminating the effects of gravity even at the edges of the PHANToM workspace. We have also successfully implemented other control strategies, such as the computed torque algorithm, that rely on the use of accurate dynamic equations.

6   Discussion

Although this paper focused on the kinematics, dynamics, and improvements of the PHANToM model 1.5, much of the results and analysis applies to other PHANToM models. Due to the similarity in the kinematics of the PHANToM models 1.0, 1.5, and 3.0, the kinematics and dynamics developed in this paper apply to models 1.0 and 3.0, with obvious variations in the parameter values. Although the theoretical transfer function model can be applied to the other models, the parameters in the actual experimental transfer function will be different.

The modifications to the motor drive electronics and velocity estimation that allowed us to realize improved performance should also apply to the 1.0 and 3.0 models. The actual implementation of these modifications for the other models will obviously need to be scaled due to the different power requirements, optical encoders, and so on. We realize that these hardware improvements have significant cost, and this cost is justified only if the highest possible performance of the mechanical device is required.

7 Future work

Although the position precision of the phantom is more than adequate, the introduction of increased position precision by means of higher-precision optical encoders will improve velocity estimation. Future work includes the mounting of sinusoidal optical encoders on the PHANToM, which will reduce the velocity granularity and improve position accuracy by a factor of 16 to 64, depending on the implementation.

It is necessary to know the acceleration of the end effector or joints of the manipulator for a variety of applications, such as teleoperation using the computed torque control algorithm. However, differentiating the already noisy and delayed velocity measurements is not feasible with the stock PHANToM configuration, or even with the additional velocity estimation electronics. We are planning to install a three-DOF MEMS accelerometer, such as the TAA3102 triaxial low-G accelerometer by NeuwGhent Technologies (LaGrangeville, NY), that will directly provide acceleration information. Furthermore, this sensor information can easily be integrated and used to estimate the velocity more accurately. It may also be feasible to determine acceleration from velocity if we implement sinusoidal encoders, improving the velocity information to a point at which it can be differentiated without too much noise.

Acknowledgments
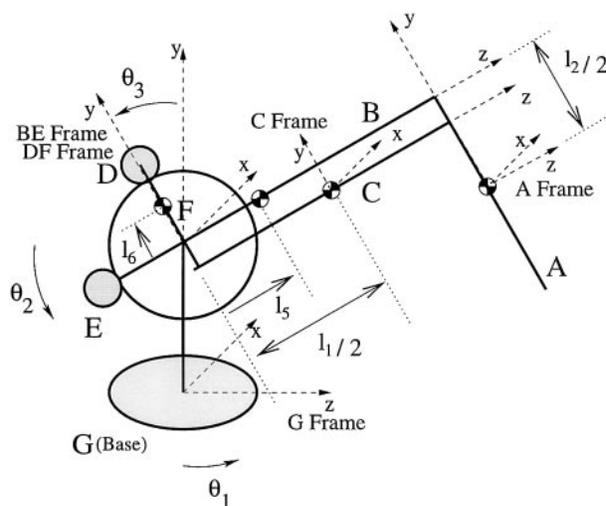
Figure 7. *Segments used in dynamics analysis.*

Appendix

Inertial Parameters

For ease of analysis, segment A through G are identified in figure 7. Note that the spatial frame used in the dynamics calculations is centered at a different point than the one used in the kinematic analysis. This is to simplify calculations, and does not affect the results.

To calculate the inertial parameters, the manipulator is assumed to be made of aluminum (with several exceptions), with a density of 1750 kg/m^3. The inertia of the motors is also included in the calculations, and the motors are assumed to be Maxon RE-025-055035.

The following parameters of the manipulator are measured as

$$l_1 = 0.215$$

$$l_2 = 0.170$$

$$l_3 = 0.0325 .$$

The inertial parameters of segment A, namely the mass of segment A and its rotational inertia matrix are estimated to be

$$m_a = 0.0202$$

$$I_a = \begin{bmatrix} I_{axx} & 0 & 0 \\ 0 & I_{ayy} & 0 \\ 0 & 0 & I_{azz} \end{bmatrix}$$

$$I_{axx} = 0.4864 \times 10^{-4}$$

$$I_{ayy} = 0.001843 \times 10^{-4}$$

$$I_{azz} = 0.4864 \times 10^{-4} .$$

For segment C, the parameters are estimated as

$$m_c = 0.0249$$

$$I_c = \begin{bmatrix} I_{cxx} & 0 & 0 \\ 0 & I_{cyy} & 0 \\ 0 & 0 & I_{czz} \end{bmatrix}$$

$$I_{cxx} = 0.959 \times 10^{-4}$$

$$I_{cyy} = 0.959 \times 10^{-4}$$

$$I_{czz} = 0.0051 \times 10^{-4} .$$

Segment BE is the combination of segment B and segment E, which is the motor actuating axis 2. Motor inertia has been added to the inertia around the x axis with a transmission ratio of 11.6:1.0. Then, the total mass of segment BE and its rotational inertia matrix are estimated to be

$$m_{be} = 0.2359$$

$$I_{be} = \begin{bmatrix} I_{bexx} & 0 & 0 \\ 0 & I_{beyy} & 0 \\ 0 & 0 & I_{bezz} \end{bmatrix}$$

$$I_{bexx} = 11.09 \times 10^{-4}$$

$$I_{beyy} = 10.06 \times 10^{-4}$$

$$I_{bezz} = 0.591 \times 10^{-4} .$$

The location of the center of mass of the segment BE is calculated as

$$l_5 = -36.8 \text{ mm}.$$

Segment DF is the combination of segment D, which is the motor actuating axis 2, and segment F. The total mass of segment DF and its rotational inertia matrix are estimated as

$$m_{df} = 0.1906$$

$$I_{df} = \begin{bmatrix} I_{df_{xx}} & 0 & 0 \\ 0 & I_{df_{yy}} & 0 \\ 0 & 0 & I_{df_{zz}} \end{bmatrix}$$

$$I_{df_{xx}} = 7.11 \times 10^{-4}$$

$$I_{df_{yy}} = 0.629 \times 10^{-4}$$

$$I_{df_{zz}} = 6.246 \times 10^{-4}$$

Motor inertia has been added to the inertia around the x axis with a transmission ratio of 11.6:1.0. The location of the center of mass of the segment DF is estimated as

$$l_6 = 52.7 \text{ mm}.$$

The only component of the rotational inertia matrix of the base that is of interest is calculated as

$$I_{base_{yy}} = 11.87 \times 10^{-4} ,$$

which includes the motor rotor inertia observed through the transmission ratio of the rotary mechanism.

References

Çavuşoğlu, M. C., & Feygin, D. (2001). *Kinematics and dynamics of PHANToM(TM) model 1.5 haptic interface*. University of California at Berkeley, Electronics Research Laboratory memo M01/15.

Çavuşoğlu, M. C., Sherman, A., & Tendick, F. (2002). Design of bilateral teleoperation controllers for haptic exploration and telemanipulation of soft environments. *IEEE Transactions on Robotics and Automation,* 18(4) (to appear).

Çavuşoğlu, M. C., & Tendick, F. (2000). Multirate simula-

tion for high fidelity haptic interaction with deformable objects in virtual environments. *Proceedings of the IEEE International Conference on Robotics and Automation (ICRA 2000),* 2458–2465.

Craig, J. J. (1989). *Introduction to robotics* (2nd ed.). Reading, MA: Addison-Wesley.

Dhruv, N., & Tendick, F. (2000). Frequency dependence of compliance contrast detection. *Proceedings of the Symposium on Haptic Interfaces for Virtual Environment and Teleoperator Systems, Part of the ASME Int'l Mechanical Engineering Congress and Exposition (IMECE 2000),* DSC 69-2, 1087–1093.

Feygin, D., Keehner, M., & Tendick, F. (2002). Haptic guidance: Experimental evaluation of a haptic training method for a perceptual motor skill. *Proceedings of the 10th Symposium on Haptic Interfaces for Virtual Environment and Teleoperator Systems (HAPTICS 2002),* 40–47.

Lemkin, M., Yang, P. H., Huang, A. C., Jones, J., & Auslander, D. M. (1995). Velocity estimation from widely spaced encoder pulses. *Proceedings of the American Control Conference, 1,* 998–1002.

Massie, T. H., & Salisbury, J. K. (1994). The PHANToM haptic interface: A device for probing virtual objects. *Proceedings of the ASME Winter Annual Meeting, Symposium on Haptic Interfaces for Virtual Environment and Teleoperator Systems,* 295–302.

Murray, R. M., Li, Z., & Sastry, S. S. (1994). *A mathematical introduction to robotic manipulation.* Boca Raton, FL: CRC Press, Inc.

SensAble Technologies, Inc. (1997). *PHANToM haptic interface hardware installation and technical manual* (revision 5.1).

Sherman, A., Çavuşoğlu, M. C., & Tendick, F. (2000). Comparison of teleoperator control architectures for palpation task. *Proceedings of the ASME Dynamic Systems and Control Division, Part of the ASME International Mechanical Engineering Congress and Exposition (IMECE 2000),* 2, 1261–1268.